# Zn²⁺-Induced Folding of RNA to Produce Honeycomb-like RNA-Mediated Fluorescing Zn²⁺/PbSe Nanostructures

Anil Kumar* and Bhupender Singh

Department of Chemistry, Indian Institute of Technology Roorkee, Roorkee 247667, India

S Supporting Information

ABSTRACT: This paper presents the synthesis of RNA-templated Zn²⁺/PbSe nanostructures following a colloidal approach. The nucleation and growth of PbSe on RNA matrix in the presence of Zn²⁺ and Pb²⁺ produces the porous Zn²⁺/PbSe building blocks through intramolecular folding, which in the process of self-assembly forms a honeycomb-like structure encapsulating Q-PbSe confined in the pores through intermolecular interactions. These nanostructures exhibit dual fluorescence in red and NIR regions at 806 nm (Φ_f = 0.01) and 1050 nm (Φ_f = 0.5), respectively. CD analysis reveals that Zn²⁺ induces the folding of RNA in the RNA-templated Zn²⁺/PbSe possibly involving the transformation from its B to A form. IR and NMR spectroscopy indicate an interaction of different components of RNA. An increase in the porosity with enhanced NIR absorption coefficient and fluorescence in the wavelength range of 900−1150 nm suggests the applications of these materials in the areas of sensing, biomedical, fluorescence imaging of tissues and for the incorporation dyes to enhance their light-harvesting capability.
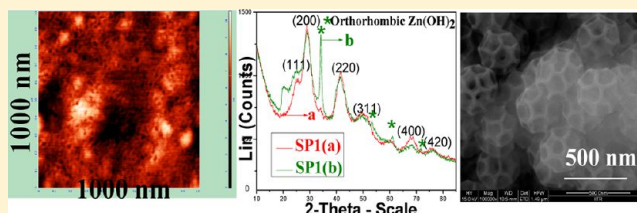
1. INTRODUCTION

In recent years a large number of investigations have focused on the synthesis of colloidal semiconducting nanomaterials absorbing light in the visible and NIR range for their potential in the fabrication of solar energy conversion devices,[1−5] photodetectors,[6,7] telecommunication[8] and biomedical applications.[9,10] In this context, lately, a specific emphasis has been laid down on IV−VI (PbS, PbSe, and PbTe) semiconductors covering wide range of light absorption in visible[11−13] and NIR range[14−16] of the solar spectrum.[17] Moreover, their large excitonic Bohr radius would not only allow to modulate their optical and photophysical properties but also could be more promising for the fabrication of nanostructures with much stronger confinement compared to II−VI and III−V materials.

The integration of biomolecules having size compatibility with nanosized semiconductor may lead to the formation of new nanostructures with functionality of biomolecule along with the properties of the core semiconductor.[11−14,18−26] Among these, the nucleic acids have been considered to be highly promising with large functionalities of nitrogenous bases and backbone, which may allow supramolecular bonding through aromatic moiety, hydrogen bonding, weak van der Waals, and electrostatic interactions. A lot of work has been contributed on the synthesis of DNA-mediated nano-hybrids;[19,24−26] however, relatively much less work has been carried out on RNA-templated nanosystems.[11−14,22]

RNA has large structural commonality with DNA except that it consists of the 2′-OH group on ribose sugar and thymine is replaced by uracil, besides being present largely as a single strand. Due to the presence of negative charge on RNA, different metal ions may influence its three-dimensional architecture significantly with regard to their folding and stabilization.[27] Ennifer et al.[28] have reported differing binding strengths and stability order for a number of alkaline earth and d-block cations for RNA strand. Among these, Mn²⁺, Zn²⁺, and Co²⁺ have been observed to undergo inner-sphere coordination specifically to Hoogsteen sites of guanines. In view of these characteristic features of RNA, the present work explores the effect of Zn²⁺ on the nanoarchitecture of RNA-mediated PbSe and also examines its photophysics. Zn²⁺ ions are known to control various metabolic activities by binding to nucleic acids in living systems.[29] Binding of these ions to the RNA matrix induces its folding in RNA-mediated PbSe to produce the quantized PbSe encapsulated in the porous nanostructure as a building block with changed optical properties. These building blocks in the process of self-assembly yield the honeycomb-like supernanostructure.

2. EXPERIMENTAL SECTION

2.1. Reagents. Ribonucleic acid derived from Torula yeast type VI (RNA), Nile blue, and Se powder (99.99%, 100 mesh) (Sigma); nitrogen gas (Grade 1, purity >99.99%) (Sigma, India), lead acetate (Qualigens), sodium hydroxide and sodium borohydride (Merck), zinc acetate (Fluka), styryl 13 (Exciton), and all other chemicals were of analytical grade and used as received.

The RNA sample used contained a heterogeneous mixture of RNA molecules of varied molecular weight(s) and length(s), and no specific sequence was employed.

2.2. Equipment. Optical absorption spectra were recorded on Shimadzu UV-2100S and Cary 5000 spectrophotometer in 1 cm quartz cell. Steady-state fluorescence was measured on a Horiba Jobin Yvon Nanolog spectrofluorophotometer equipped with 450 W xenon lamp source. X-ray diffraction patterns were obtained on a Bruker AXS D8 Advance X-ray diffractometer (XRD) using Cu Kα line (1.5418 Å) at 40 kV and 30 mA. The diffraction patterns were recorded in 2θ range of 10°−90° at a slow scan rate of 0.02°/step and 0.5 s per step. X-ray photoelectron spectroscopy (XPS) data were recorded on an AXIS-His Kratos Analytic Inc. instrument using a Mono Aluminum probe beam.

Surface morphology was analyzed by recording 2D and 3D images of fresh and aged samples of the colloidal solutions by the drop casting method using tapping mode of atomic force microscope (AFM) supplied by M/s Molecular Tools and Devices for Nanotechnology (NT-MDT). AFM was equipped with NOVA software for image analysis. Surface topography was also examined on a QUANTA 200-FEG digital field emission scanning electron microscope (FE-SEM) equipped with CCD camera, and elemental analyses of the synthesized nanosystems at various locations were performed using the energy-dispersive X-ray analysis (EDAX) accessory. Electron micrographs along with selected area electron diffraction were recorded on a FEI-TECNAI 300 kV digital transmission electron microscope (TEM) equipped with EDAX facility having resolution of 0.19 nm.

IR spectra were measured in mid-IR range (4000−400 cm^{-1}) in KBr medium on a Thermo Nicolet Nexus FTIR spectrophotometer and processed by OMNIC v6.1 software. The proton NMR spectra were recorded on a Bruker Avance 500 (500 MHz) spectrometer in H_2O and D_2O media. Circular dichroism (CD) spectra of the as-synthesized samples were recorded on a Chirascan spectropolarimeter supplied by M/s Applied Photophysics, UK. The ellipticity of the as-prepared colloidal samples have been reported by subtracting the baseline of used water as solvent for preparing samples in a 500 μL cuvette from 200 to 320 nm.

2.3. Synthesis of RNA-Capped Zn^{2+}/PbSe Samples. Zn^{2+}/PbSe nanostructures in RNA matrix were synthesized under inert environment at 4 °C by maintaining the pH of 8.5 at each step. In all the samples containing Zn^{2+}, Zn^{2+} solution was added prior to addition of Pb^{2+} or precipitation of PbSe solution.

Colloidal PbSe containing varied amounts of Zn^{2+} (1.0− 15.0) × 10^{-5} mol dm^{-3}) was prepared by adding 150 μL of 0.1 mol dm^{-3} lead acetate to the deaerated solution of RNA (0.022 g/100 mL). It was followed by the quick injection of freshly prepared NaHSe from the sides of the vessel under vigorous stirring.[13] The resulting mixture turns reddish brown instantaneously and was purged with nitrogen gas strongly for about 10 min followed by the dropwise addition of 150 μL of 0.1 mol dm^{-3} excess Pb^{2+} solution from its stock solution to makeup the effective concentrations of PbSe and Pb^{2+} at 1.5 × 10^{-3} mol dm^{-3} each and Pb/Se = 2.

2.4. Methodology. Samples for atomic force microscope (AFM) were prepared by applying sample sizes of about 15 μL on a glass plate, which was subsequently dried at room temperature. For these experiments, the scanning frequency

was varied in the range of 1.5−3.13 Hz and data were recorded at room temperature (20 ± 2 °C).

Samples for TEM analysis were prepared by applying a drop of the colloidal sample on a carbon-coated copper grid G-200 (size 3.05 mm). The excess of colloidal solution was removed with the help of a tissue paper. The coated grid was dried in dark at room temperature for about 30 min to evaporate the remaining moisture. Electron micrographs of these samples were recorded by scanning the dried grid at different magnifications under the electron microscope at an accelerating voltage of 300 kV. Selected area electron diffraction (SAED) patterns of the colloidal samples were recorded to find out the structure of different phases in the colloids samples. Indexing of electron diffraction pattern was carried out using a ratio method, and Miller indices were then assigned corresponding to different rings.

Samples for field emission scanning electron microscopy (FESEM) and EDAX analysis were prepared by applying about 3 times higher sample size(s) (∼40 μL) compared to those employed for AFM and TEM analysis. At lower sample size, a burning of sample was noted even after reducing the voltage down to 15 kV. For X-ray diffraction (XRD), X-ray photoelectron spectroscopy (XPS), and infrared (IR) measurements, solid material(s) of the as-prepared samples were obtained by removing excess of water on a Buchi R-114 Rotavapor at 35 °C from their colloidal solution(s).

ImageJ software was used for image analysis. It was specifically used for 3D viewing of holes/pits/pores in the nano/microstructures recorded by FESEM and TEM. NOVA software was used for analyzing the hole/pore/grain size of the AFM images.

3. RESULTS

3.1. Characterization of Zn^{2+}-Induced RNA-Mediated Zn^{2+}/PbSe Nanostructures. *3.1.1. Optical Absorption and*
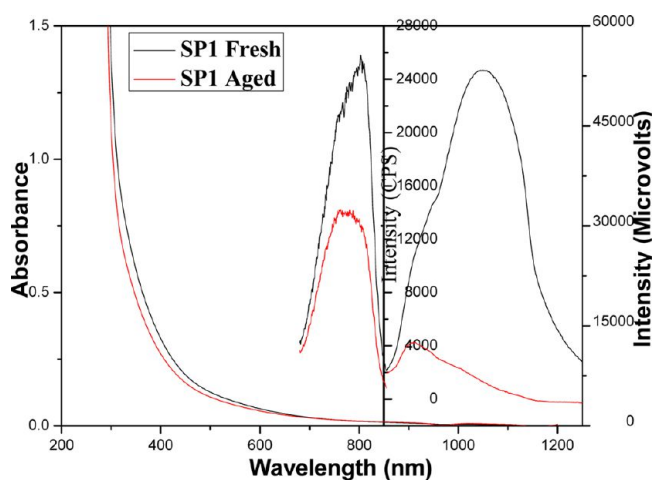
Figure 1. Optical absorption and fluorescence spectra of SP1: fresh (black) and aged (red).

Fluorescence. Optical absorption spectrum of fresh colloidal PbSe was optimized by varying the amounts of Zn^{2+} (1.0 × 10^{-5} to 10 × 10^{-5} mol dm^{-3}) in the UV−visible and NIR regions (200−1050 nm).

The optimization of the [Zn^{2+}] was performed by monitoring the optical absorption and fluorescence in the NIR region.[30] The optimized sample, with the highest
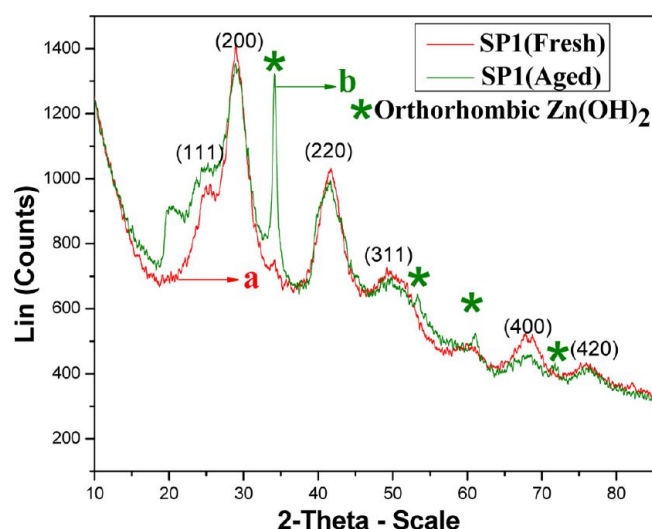
Figure 2. XRD patterns of SP1: fresh (a) and aged (b).

fluorescence efficiency in the NIR region, contained $[RNA] = 0.022$ g/100 mL, $[Zn^{2+}] = 10 \times 10^{-5}$ mol dm^{-3}, $[Pb^{2+}] = 3 \times 10^{-4}$ mol dm^{-3}, and $[HSe^-] = 1.5 \times 10^{-4}$ mol dm^{-3} at pH 8.5 and is denoted as SP1. The excitation of these nanostructures by 670 nm light radiation results in the production of fluorescence spectrum having a weak fluorescence band at 806 nm in the red region and relatively stronger fluorescence in the NIR range having a shoulder at 944 nm along with a broad fluorescence band at 1050 nm. The quantum efficiency of fluorescence in the red and NIR range were estimated to be 0.01 and 0.5, respectively. The optical absorption and fluorescence spectra of SP1 are shown in Figure 1.

For performing control experiments in the absence of PbSe, blank samples SB and SB1 were prepared. SB contained 0.022 g of RNA/100 mL at pH 8.5 and SB1 contained 0.022 g of RNA/100 mL; $[Zn^{2+}] = 10.0 \times 10^{-5}$ mol dm^{-3} and $[Pb^{2+}] = 3.0 \times 10^{-4}$ mol dm^{-3}. For SB and SB1, no change in the optical absorption spectra were observed in the absorption range beyond 370 nm (not shown), indicating the observed change in
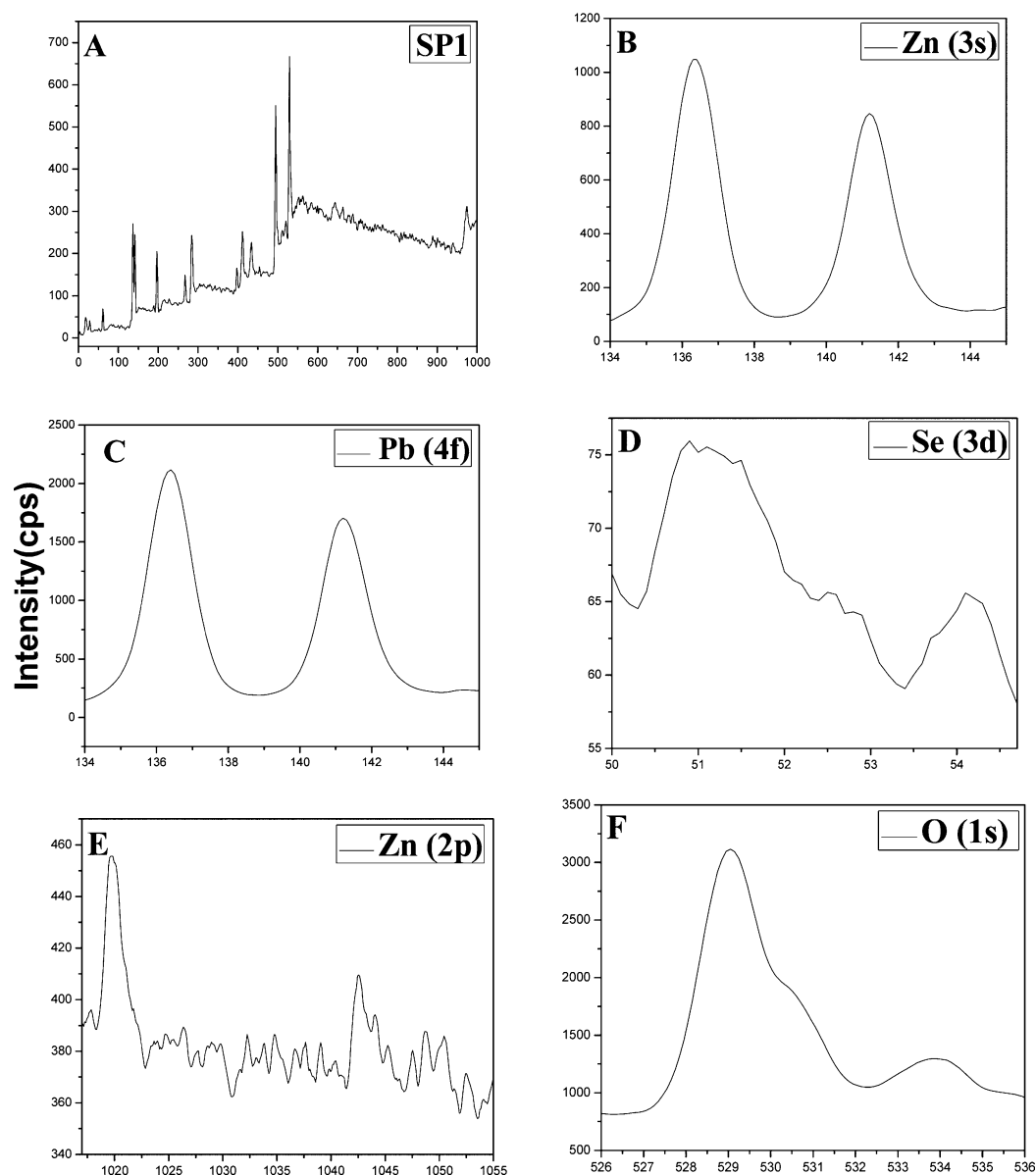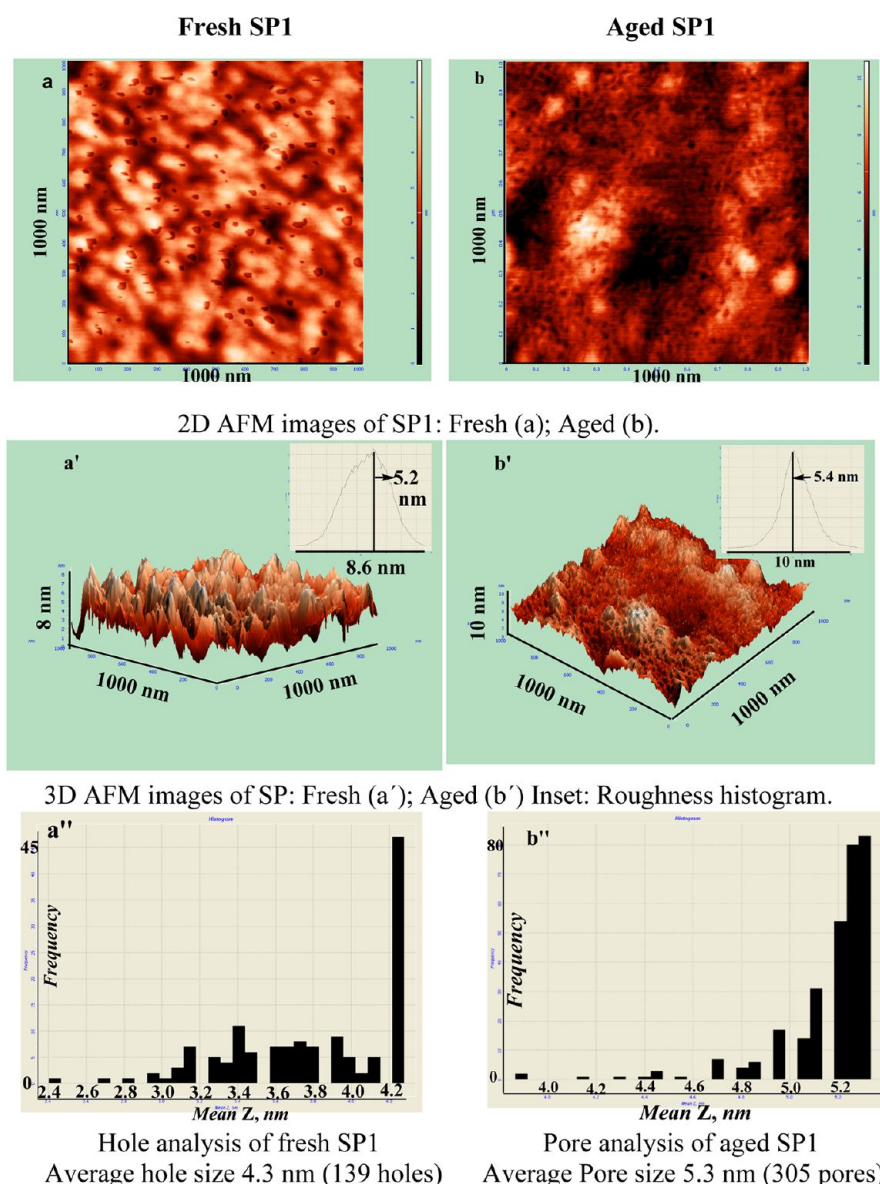

Figure 3. X-ray photoelectron spectra of SP1.

5388

dx.doi.org/10.1021/jp309822w | J. Phys. Chem. C 2013, 117, 5386–5396

Fresh SP1　　　　　　　　**Aged SP1**

2D AFM images of SP1: Fresh (a); Aged (b).

3D AFM images of SP: Fresh (a′); Aged (b′) Inset: Roughness histogram.

Hole analysis of fresh SP1
Average hole size 4.3 nm (139 holes)

Pore analysis of aged SP1
Average Pore size 5.3 nm (305 pores)

Figure 4. AFM images of SP1: Fresh (a, a′, a″); Aged (b, b′, b″).

the absorption spectrum of SP1 to arise by the interaction of Zn^{2+} with PbSe.

Aging caused a reduction in the absorbance in the entire UV−vis−NIR range (Figure 1). The fluorescence due to aged SP1, however, depicted a blue shift in the fluorescence bands in the red and NIR ranges from 806 nm (1.54 eV) to 769 nm (1.61 eV), and 944 nm (1.31 eV) and 1050 nm (1.18 eV) to 905 nm (1.37 eV) and 1006 nm (1.23 eV), respectively, with a significant reduction in the fluorescence intensity (Figure 1).

3.1.2. XRD. XRD patterns of fresh and aged SP1 (Figure 2) display various prominent reflections corresponding to (111), (200), (220), (311), (400), and (420) planes matching to the face-centered-cubic (fcc) structure of PbSe (JCPDS file No. 06-0354).[31] Besides this, it also exhibits a very weak reflection at d value of 2.62 Å, which does not correspond to the PbSe phase. Aging of these samples, however, depicted various additional peaks corresponding to 2θ (d spacing in Å): 19.69 (4.51), 34.16 (2.62), 61.15 (1.51), and 71.89 (1.31) values matching the $Zn(OH)_2$ phase with the orthorhombic structure (ICSD ref. No. 00-012-0479). Moreover, peaks corresponding to the PbSe

phase now became slightly broader and less intense indicating the change in the size/morphology of the nanostructure. A small peak noted above in the fresh SP1 at 2θ (d spacing in Å) value of 34.16 (2.62) corresponds to one of the most intense peaks observed for the $Zn(OH)_2$ phase.

3.1.3. XPS. In order to probe the presence of Zn and Pb species in the as-prepared sample, X-ray photoelectron spectrum (XPS) of SP1 was recorded (Figure 3). This spectrum is dominated by two peaks at 136.4 and 141.2 eV (Table S1 in the Supporting Information) corresponding to doublet of Pb arising from the $4f_{5/2}$ and $4f_{7/2}$ spin−orbital coupling. Interestingly, these bands are observed in the lower energy range and there was no higher energy band/shoulder corresponding to Pb−O or its adduct(s) as have been observed earlier for air-exposed samples of PbSe at nearly 138 and 144 eV.[32]

This clearly indicates the absence of oxidation of PbSe in the present case. Two broad peaks observed at 51.2 and 54.1 eV correspond to the 3d level of the selenium. Besides, O 1s peaks were observed at 529.1 and 534 eV (Table S1), which were

5389

dx.doi.org/10.1021/jp309822w | J. Phys. Chem. C 2013, 117, 5386−5396
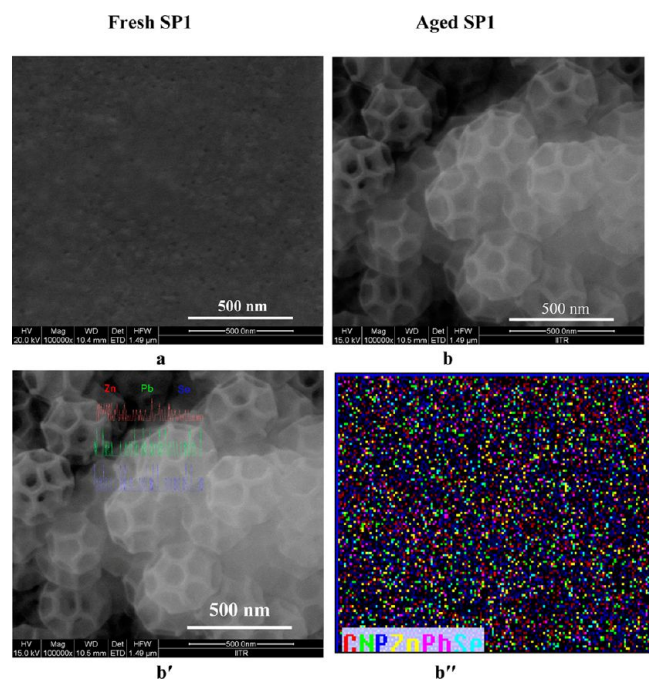
Figure 5. FESEM Images of SP1: fresh (a) and aged (b). Elemental mapping of aged SP1 (b′). Area mapping of FESEM image shown in panel b (b″).

earlier identified for $Pb(OH)_2$ and $Zn(OH)_2$ species, respectively.[32,33] A shoulder at 530.6 eV was similar to that observed in Pb^{2+} containing $PbSe^{34}$ in the absence of Zn^{2+} and might be assigned to the presence of other hydrated Pb^{2+} species under the experimental conditions used. These studies indicate that SP1 contains PbSe besides $Zn(OH)_2$, $Pb(OH)_2$, and hydrated Pb^{2+} species.

3.1.4. AFM Analysis. 2D and 3D atomic force microscopy (AFM) images of fresh and aged SP1 are shown in Figure 4. 2D image of fresh SP1 shows these nanostructures to have pits/holes of varied size and depth. Analyses of these nanostructures give the average maximum surface roughness (roughness distribution) of 5.2 nm (0.5−8.5 nm) and the hole size (number of holes) of about 4.3 nm (139) (Figure 4a,a′,a″, and Table S2 in the Supporting Information).

Aging of SP1 brings a peculiar change in their morphology, which now shows the presence of clusters of building blocks observed for the fresh SP1 eventually assuming porous honeycomb-like structure matching the shape of buckyballs. Aging increases the average maximum surface roughness (roughness distribution) to 5.4 nm (3.0−10.4 nm) along with the pore size (number of pores) to about 5.3 nm (305) (Figure 4b,b′,b″, and Table S2 in the Supporting Information). The depth profiles of the fresh and aged AFM images of SP1, given in Figure 4, a and b, were recorded along the X and Y axes and are shown in Figure S1a−S1d in the Supporting Information. Data of depth and pore analysis are presented in Table S2.

The participation of Zn^{2+} in the development of porous nanostructures was further analyzed by investigating the effect of $[Zn^{2+}]$ (1×10^{-5} to 15.0×10^{-5} mol dm^{-3}) on the size and morphology of Zn^{2+}/PbSe nanostructure using AFM. An increase in the concentration of Zn^{2+} from 1×10^{-5} to 2.5×10^{-5} mol dm^{-3} produces largely spherical nanoparticles with increasing average maximum surface roughness (roughness distribution) from 6.6 nm (1.8 to 13.7 nm) to 8.8 nm (3.0 to 18 nm). An increase in $[Zn^{2+}]$ to 5×10^{-5} creates some holes and

these nanostructures depicted the average maximum surface roughness (roughness distribution) of 13 nm (3.0−25.0 nm) (Figure S2a−S2c in the Supporting Information). For a typical Zn^{2+} concentration of 10×10^{-5} mol dm^{-3}, it shows nanostructures with fairly large number of pits/holes as discussed above (Figure 4). A further increase in Zn^{2+} to 15×10^{-5} mol dm^{-3}, however, produces the organized chains without any porosity with average maximum surface roughness (roughness distribution) of 19 nm (8 to 34 nm) (Figure S2d). These experiments clearly reveal that there is a regular change in morphology with varied Zn^{2+} and a specific concentration of Zn^{2+} is responsible for forming the hollow structure.

In control experiments, AFM images were also recorded for both fresh and aged RNA $(SB)^{14}$ and RNA containing Zn^{2+} and Pb^{2+} (SB1) (Figure S3A,B,C in the Supporting Information). The AFM image of SB shows the formation of spherical nanoparticles having an average maximum surface roughness (roughness distribution) of 7.8 nm (3.7−18.0 nm), which upon aging shows the formation of bigger clusters with an average maximum surface roughness (roughness distribution) of 9.8 (0.8−21 nm). The AFM image of fresh SB1 exhibits a slight porous structure (Figure S3A-a) with an average maximum surface roughness (roughness distribution) of 2.7 nm (0.4−5.7 nm) (Figure S3B-a and Table S3 in the Supporting Information). Aging of these nanoparticles shows the chains of more organized structure containing folded nanowires (Figure S3A-a′). In this case, average maximum surface roughness (roughness distribution) is slightly reduced to 2.6 nm (0.4−5.2 nm) compared to those observed for the fresh SB1.

Thus, a comparison of AFM images in the absence (Figure S3) and presence of PbSe (Figure 4) clearly demonstrates a difference in the morphology in the two cases and the changes observed in SP1 arise by the interaction of Zn^{2+} and Pb^{2+} ions with RNA-mediated PbSe and not with the interactions of Zn^{2+} and Pb^{2+} ions with RNA alone.

3.1.5. FESEM Analysis. FESEM images of fresh and aged SP1 are recorded in Figure 5. The image of fresh SP1 shows the presence of holes distributed randomly and EDAX analysis of these nanostructures at various locations shows the presence of Pb, Se, and Zn along with C, N, and P (Figure 5a, and Figure S4a,b in the Supporting Information). These colloidal nanostructures upon aging in SP1 undergo a hierarchical organization to give honeycomb-like porous structure resembling the buckyball (Figure 5b). Elemental and area mapping of aged SP1 are given in Figure 5, b′ and b″, respectively. It demonstrates a homogeneous distribution of Zn, Pb, Se, C, N, and P all along the micrograph. EDAX analysis of buckyball at its various locations, i.e., inside and outside the pores, also show the presence of Pb, Se, and Zn along with C, N, and P (Figure S4c,d in the Supporting Information). These observations suggest that different building blocks of SP1 in the fresh sample undergo intermolecular interactions to yield a more organized packed structure in the process of self-assembly.

3.1.6. TEM Analysis. HRTEM micrographs of fresh and aged SP1 along with their SAED and EDAX analyses are given in Figure 6.

TEM image of fresh SP1 shows these nanostructures to be slightly porous as some holes could be seen from its 3D view using imageJ software (Figure S5a in the Supporting Information). SAED pattern of this image depicts diffused rings. Indexing of SAED pattern shows these rings correspond to reflections from (111), (200), (220), and (311) planes
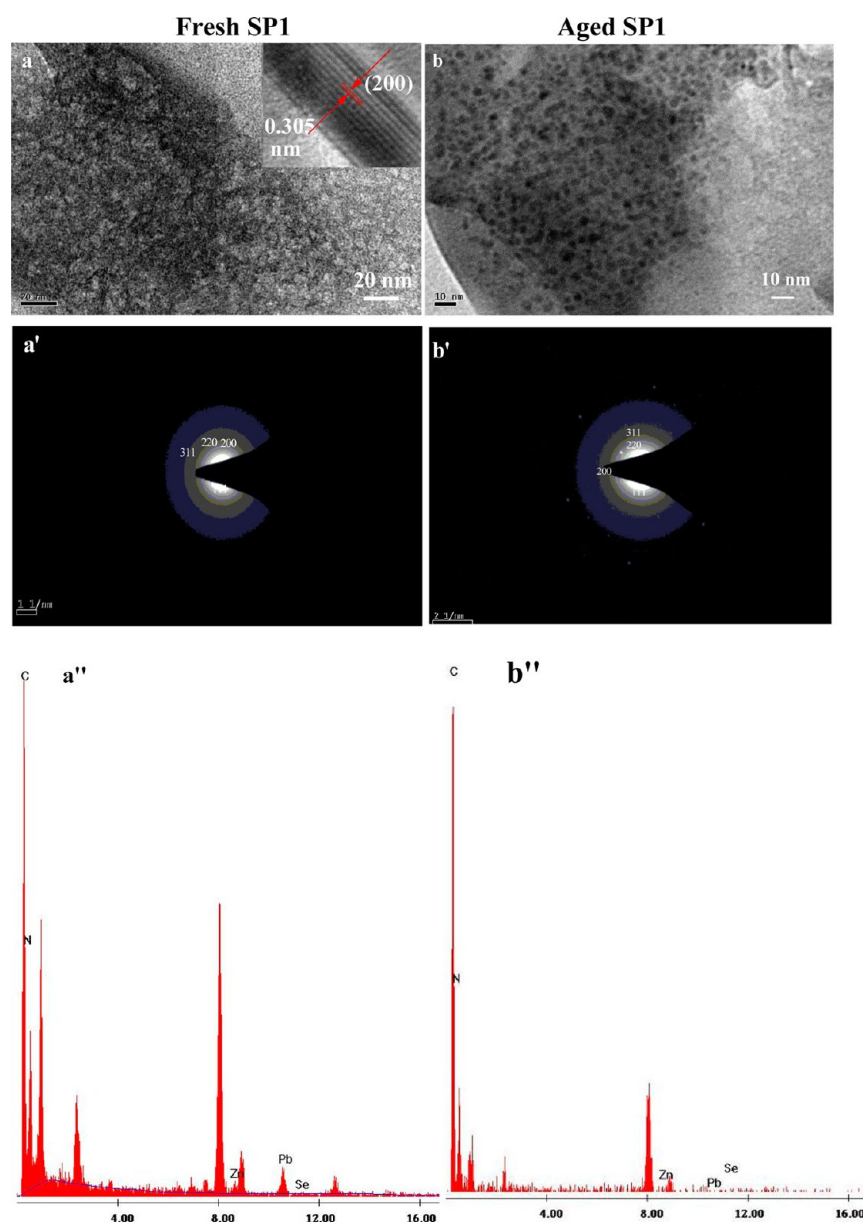
Figure 6. HRTEM micrographs, SAED patterns, and EDAX spectra of SP1: fresh (a,a′,a″) and aged (b,b′,b″).

matching to PbSe in fcc phase. Aging of SP1 results in a morphological change of these nanostructures, which at high resolution exhibit an organized honeycomb-like structure containing bigger pores (Figure 6). 3D viewing of this micrograph evidently shows a number of homogeneously distributed pores of fairly bigger dimension on the surfaces of this nanostructure (Figure S5a′). These pores are much denser compared to those observed in the fresh image (Figure S5a). Analysis of SAED pattern of the aged sample depicts highly diffused rings without distinct boundaries. EDAX analysis of the micrographs of fresh and aged samples indicates the presence of Zn, Pb, and Se along with C and N, the constituents of RNA (Figure 6).

3.1.7. FTIR Analysis. IR spectra of pure RNA (SB), RNA matrix in the presence of Pb^{2+} (3.0×10^{-4} mol dm^{-3}) and Zn^{2+} (1.0×10^{-4} mol dm^{-3}) (SB1), and SP1 are presented in Figure 7, a, b, and c, respectively, and their respective spectral data have been recorded in Table S4 in the Supporting Information.

IR spectrum of SB depicts all the characteristic peaks due to RNA.[35]

A careful comparison of the IR spectra of SB and SB1 with SP1 reveals a significant difference among them with regard to shape and positions of vibration band(s) corresponding to different nitrogenous bases observed in SB. A specific comparison of SB1 and SP1 containing the same amount of Zn^{2+} and Pb^{2+}, except the latter also containing PbSe, shows an interaction of purine bases A and C, U, C, in-plane C2′−OH, purines in syn conformation, asymmetric stretches due to PO_2^{2-} and RNA backbone with Zn^{2+} and Pb^{2+} as well as with PbSe. It is pertinent to point out that the vibrational band due to G disappeared even in the absence of PbSe in SB1, but the band due to U shows a remarkable change in both position and shape for both SB1 and SP1 compared to SB. A band at 1070 cm^{-1} observed for SB, assigned to furanose for CO stretch of backbone, is increasingly blue-shifted in the order SB < SB1 < SP1, suggesting it to be involved in the interaction with Zn^{2+} and Pb^{2+} as well as with PbSe.

5391

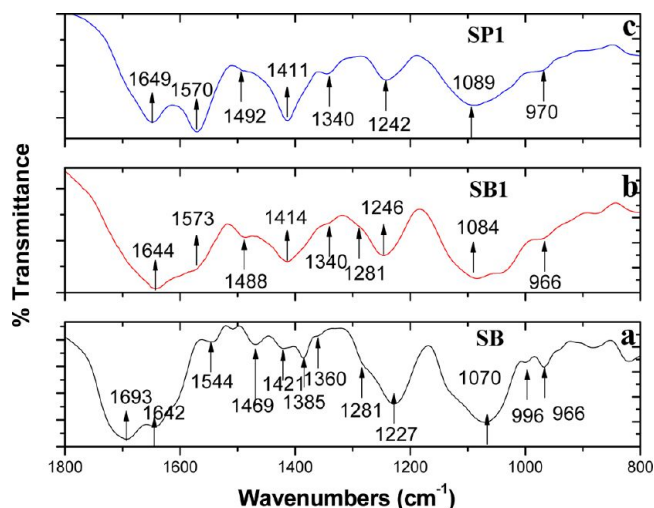dx.doi.org/10.1021/jp309822w | J. Phys. Chem. C 2013, 117, 5386−5396

Figure 7. Mid-IR spectra of SB (a), SB1 (b), and SP1(c).

SB shows a peak at 966 cm^{-1} corresponding to RNA backbone. This peak gets broadened in SB1 and is shifted to 970 cm^{-1} in SP1. The peak at 1227 cm^{-1}, present mainly in the B form of RNA, is shifted to higher energy at 1244 cm^{-1} for SB1 and then to 1242 cm^{-1} along with a change in the shape for SP1. These observations suggest that RNA in SP1 gets converted from B to A form.[35] Details of the changes in the peak position, their shape, and disappearance of certain peaks are included in Table S4 in the Supporting Information. These observations evidently indicate interaction of different moieties of RNA with Zn^{2+}/PbSe.

3.1.8. NMR Studies. The sites of interaction for Pb^{2+}, Zn^{2+}, and PbSe with RNA matrix were also analyzed by recording proton NMR spectra of SB1 and SP1 (Figure 8). NMR spectral data of these samples are compiled in Table S5 in the Supporting Information. NMR spectrum of SB[14] exhibited all the charactericstic peaks due to protons of different moieties of RNA, namely, sugar (3.6–4.5 ppm), sugar and purine base (5.5–6.2 ppm), and purine and pyrimidine bases (7.5–8.4 ppm) as reported earlier[36] for RNA.

A comparison of the ^{1}H NMR spectra (Figure 8a) of SB1 with SP1 shows a downfield shift in the resonance absorption due to protons of different moieties of RNA to higher values of δ (ppm) as given in Table S5. It shifted the resonance absorption of protons (ppm) corresponding to 2′-OH from 1.80 to 1.93; sugar protons from (4.35–3.41) to (4.49–3.75); bases and sugar protons from (5.70–5.98) to (5.83–6.07); and aromatic protons of purine and pyrimidine bases from (7.63–8.33) to (7.65–8.46), respectively. The observed downfield shift in SP1 compared to that of SB1 is understood due to reduced electron density at various sites because of increased interactions in the presence of Zn^{2+}/Zn(OH)$_2$ and excess Pb^{2+} with PbSe.

^{31}P NMR spectra of SB1 and SP1 are presented in Figure 8b. These spectra did not exhibit any appreciable change in the shape of the peak, but the chemical shift shows a regular increase in δ (ppm) indicating an increased interaction of Zn^{2+}/Zn(OH)$_2$ through PO$_2^{2-}$ of RNA in the presence of PbSe. An increasing downfield shift in the NMR in order of SB < SB1 < SP1 (Table S5) suggests an increased interaction of phosphate group with Zn^{2+}/Pb^{2+} in the absence of PbSe, which is further increased in the presence of PbSe.

3.1.9. CD Spectra. SB1 shows three peaks, one positive peak at 273 nm and two negative peaks at 242 and 211 nm (Figure 9, and Table S6 in the Supporting Information), respectively very similar to CD spectrum of RNA extracted from yeast observed earlier.[37,38] The formation of SP1 resulted in a slight blue shift in the CD spectrum due to SB1 for both positive and negative peaks. Further, the ellipticity due to SP1 fresh is slightly higher compared to that of SB1, suggesting the absence of denaturation of RNA upon the formation of PbSe. For the aged SP1 all these peaks depict a further blue shift with a change in the nature of spectrum, in which the intensity due to all positive and negative peaks is significantly reduced associated with a more blue shift and the middle peak is slightly positive. It indicates a slight decrease in ellipticity. Such a change has earlier been reported for conversion of A DNA to B DNA.[38] In the present case, the torula yeast RNA shows a positive peak at 273 nm, which is blue-shifted and the negative middle maximum peak turning to become slightly positive upon aging. These changes are interpreted in terms of a conformational change from B form of RNA to A form in view of the previous report on A RNA having a maximum at ~260 nm.[38,39]

4. DISCUSSION

In the optical absorption spectrum of optimized Zn^{2+}/PbSe, the excitonic absorption due to PbSe becomes less prominent compared to bare PbSe.[13] A poor transition probability in the optical absorption of SP1 in the visible region possibly arises due to low density of states in the conduction band. These changes in optical absorption are associated with a simultaneous decrease in fluorescence efficiency in the red region and an increase in the NIR region. The details analysis of these changes will be presented elsewhere.[30]

A variation in the concentrations of Zn^{2+} exhibits peculiar morphological changes in AFM images of PbSe (Figure 4; Figure S2a–2d in the Supporting Information). It causes the development of the hollow structure in the fresh SP1 only; the size of the holes of these nanostructures was estimated to be 4.3 nm (Table S2 in the Supporting Information). Interestingly, either a decrease or increase in concentration of Zn^{2+} other than the optimum concentration (10 × 10^{-5} mol dm^{-3}) did not exhibit such topography; instead, the hollow structure was almost lost. It evidently indicates a correlation between the morphology and the added amount of Zn^{2+}. Thus, it is only a particular concentration of Zn^{2+}, Pb^{2+}, RNA, and PbSe corresponding to SP1, which may be termed as a building block responsible for the observed structural changes. Aging of this sample introduces in it a porous character (Figure 4b).

The binding of Zn^{2+} to SB in the presence of Pb^{2+} results in its folding to form pores in the fresh SB1 (Figure S3A). This sample upon aging is reorganized to produce nanowire-like structure possibly involving extensive intermolecular H-bonding interactions (Figure S3B), which is quite different from that observed in the presence of PbSe in aged SP1(Figures 4b, 5b, and 6b). The addition of HSe$^-$ to SB1 produces PbSe on folded RNA, which is understood to generate the hollow structure due to increased supramolecular interactions involving Zn^{2+}/Zn(OH)$_2$ in fresh SP1 (Figures 4a, 5a, and 6a). This sample reorganizes to produce the building block(s) containing unit cells on the matrix in which Pb^{2+}/Zn^{2+} and Se^{2-} are rearranged involving weak physical interactions: like van der Waals, $\pi-\pi$, polarization of Se in PbSe by Pb^{2+}/Zn^{2+}, and H-bonding. These interactions are responsible for the

5392

dx.doi.org/10.1021/jp309822w | J. Phys. Chem. C 2013, 117, 5386–5396
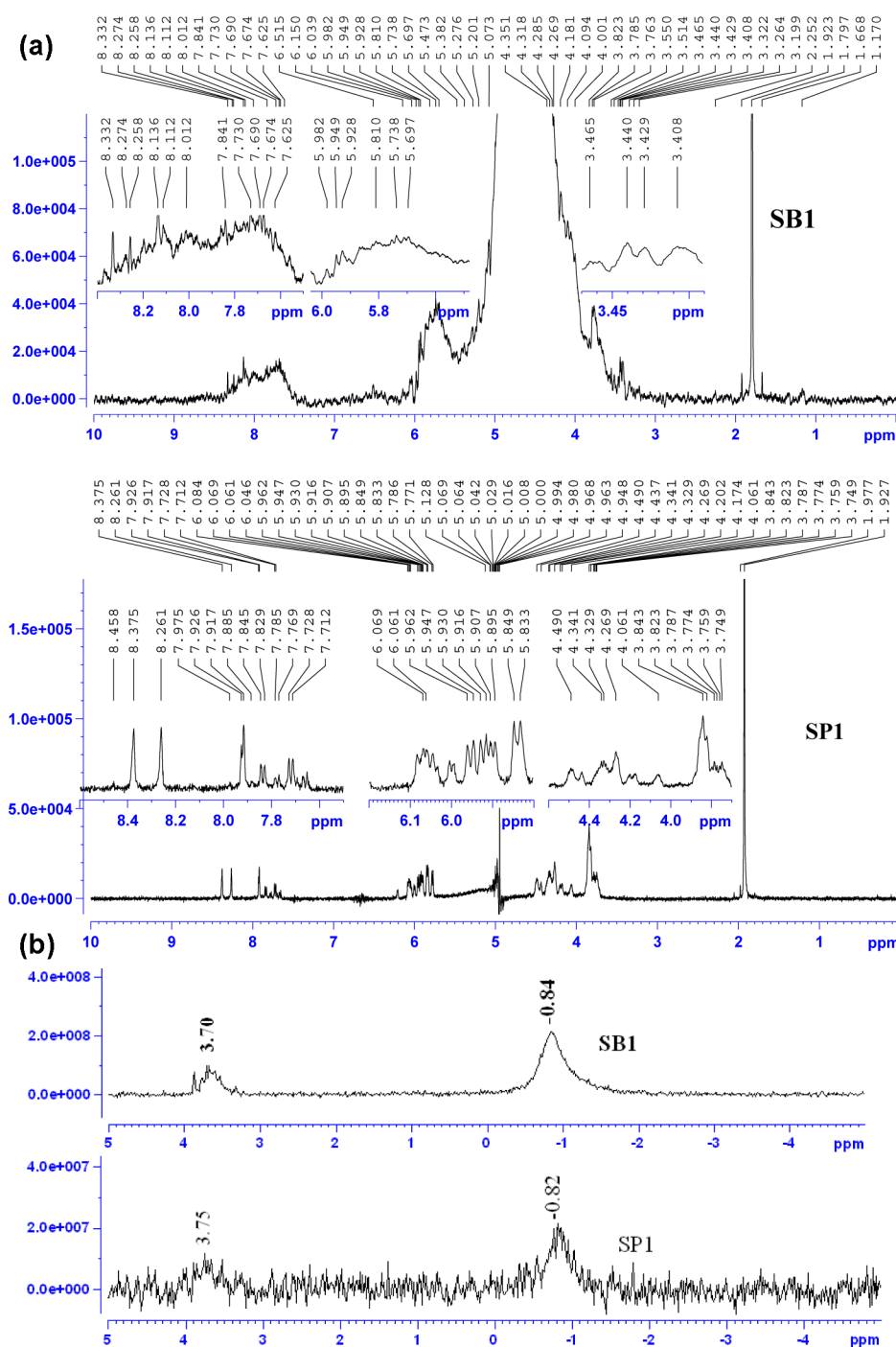
Figure 8. (a) ^1H NMR spectra of SB1 and SP1. Inset depicts expanded region in specific δ (ppm) range(s). (b) ^{31}P NMR spectra of SB1 and SP1.

formation of hollow structure in the fresh sample. The observed change in the surface topography of the aged SP1 can be attributed to the increased production of $Zn(OH)_2$, as was evidenced by XRD in which the peak due to $Zn(OH)_2$ became fairly intense for aged SP1 as compared to the fresh sample (Figure 2). The formation of $Zn(OH)_2$ enhances the supramolecular interactions through H-bonding to generate building block with relatively bigger holes/pores. In the process of self-assembly during aging, the building blocks are rearranged to yield the honeycomb-like porous structure (Figures 4b, 5b, and 6b) in order to achieve the thermodynamic stability and structural requirement of 3D packing (vide infra).

A schematic illustration of these changes is presented in Scheme 1.

The formation of the holes for the optimized concentration of Zn^{2+} and the development of honeycomb-like porous structure upon aging was evidenced by the AFM, TEM, and FESEM studies (Figures 4−6). For fresh SP1 the observed average hole size(s) by TEM is very similar to that recorded by AFM. A slightly bigger hole size observed by FESEM (10.8 nm) compared to those arrived by AFM and TEM analysis might have been contributed due to more than double the sample size used in these experiments.
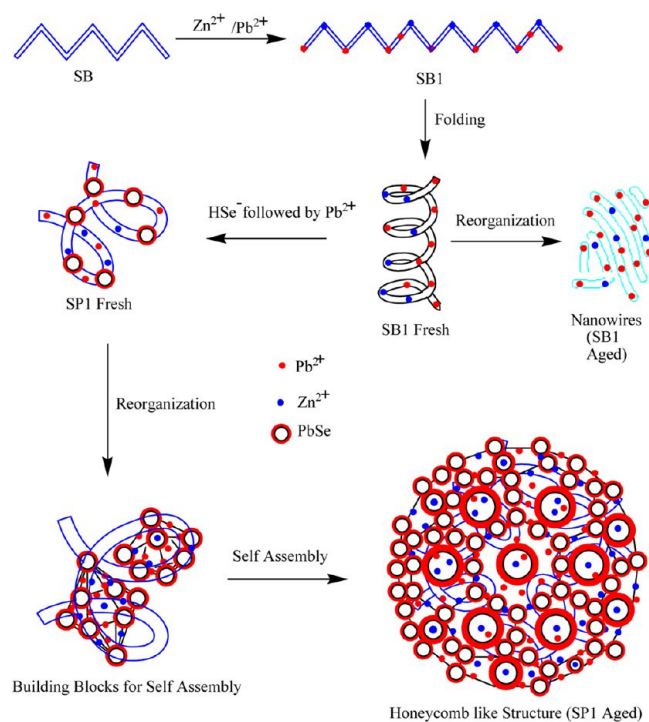
The observed Zn^{2+} concentration-dependent optical and morphological changes indicate an interaction of Zn^{2+} with
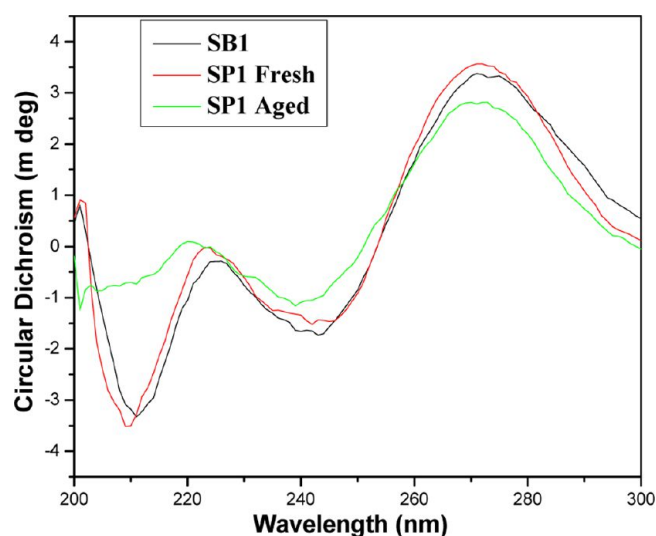
Figure 9. CD spectra of fresh SB1 (black), fresh SP1 (red), and aged SP1 (green).

Scheme 1. Schematic Illustration of the Folding of RNA To Form Porous Building Block and Honeycomb-like Supernanostructure in the Process of Self-Assembly

RNA-mediated PbSe. The fact that a typical $[Zn^{2+}]$ only contributes to the formation of porous structure in aged SP1 might be understood in view of the fixed coordination number of Zn^{2+} ion. Zn^{2+} ion binds to different moieties of RNA and PbSe through supramolecular interactions as was shown by the IR and NMR spectroscopy. In the presence of PbSe, increased interactions of Zn^{2+} and Pb^{2+} with RNA are observed compared to those in its absence (Figures 7 and 8; Tables S4 and S5). A difference in the morphology of SB1 and SP1 can be attributed to the polarization of PbSe by Zn^{2+} interacting through Se^{2-}. Zn^{2+} bound to RNA strand could induce polarization in PbSe, which would result in increased binding of Zn^{2+} to different

moieties of RNA and PbSe through supramolecular inter-actions. These interactions become more prominent through $Zn(OH)_2$ formed in the process of aging. These morphological changes for SP1 are also evidenced by AFM and electron microscopy, which demonstrate a change from hollow building block for the fresh sample to 3D honeycomb- like porous structure for the aged SP1 (Figures 4−6).

The folding of RNA strand through Zn^{2+} when bound to PbSe is also indicated by CD spectroscopy of fresh SP1, in which the positive peak for SP1 was observed almost at the same wavelength as observed for SB/SB1 having a very similar magnitude, but the negative peak gets blue-shifted. For the aged SP1, the middle peak shows a slight positive ellipticity and the blue shift becomes more prominent indicating a change in conformation of RNA from its B form to A form. This transformation might have occurred possibly due to differing interactions of Zn^{2+} under these conditions. The observations made by CD are also supported by IR spectroscopy in which a blue shift in the absorbance band due to PO_2^{2-} asymmetric stretch was observed from 1227 to 1242 cm^{-1}, which has been assigned to the suggested conformational change.[35]

The fcc structure of Zn^{2+}/PbSe in the present case suggests that in the close packing of such molecules in 3D structure may contain several such particles to form a cluster giving its 3D packed structure. Such an organization might be considered to arise due to the functionalization of Zn^{2+}/PbSe by the RNA in the nanohybrids. An urge for the formation of honeycomb-like structure is provided by the supramolecular interactions among the shells of various building blocks involving Watson−Crick and Hoogsteen interactions and the close packing requirement of the fcc structure of PbSe. The fact that a particular ratio of the metal ions is required to stabilize such structures, it is likely that these ions could be present in the tetrahedral and octahedral voids created by the fcc lattice. These ions might have facilitated the formation of honeycomb-like structure by providing interacting sites for the unit cell holding them closer to each other. The observed structural change in these nanosystems could thus be attributed to the difference in nature of interactions of metal ions with PbSe as well as with the template. Based on these data, the interactions of RNA in the absence and presence of PbSe in SP1 are given in Scheme S1 in the Supporting Information.

This nanosystem having porous nanostructures could be used to incorporate dyes like porphyrin(s)/chlorophyll etc. to enhance their light harvesting capability. This aspect was explored by interacting Zn^{2+}/PbSe nanostructures with Nile blue, a dye having spectral properties suitable for fluorescence resonance energy transfer. Since a portion of the fluorescence spectrum of Zn^{2+}/PbSe overlapped the optical absorption of Nile blue, it could thus affect the fluorescence resonance energy transfer (FRET) from PbSe (D) to the dye (A). From these experiments, it is arrived that this system could effectively sense about 10 nM of Nile blue.[40]

This paper makes use of a basic principle of folding of RNA strand induced by cation(s) and explores their binding capability for the fabrication of different architectures of RNA-mediated PbSe. In the present case, the PbSe quantum dots are produced on the Pb^{2+}/Zn^{2+}-bound RNA scaffold. Zn^{2+} ions induce the folding of RNA in RNA-mediated Zn^{2+}/PbSe to yield the hollow nanohybrid(s) containing PbSe in the core. These building blocks in the process of self-assembly produce honeycomb-like porous structure involving weak electrostatic, H-bonding, and van der Waals type supramolecular interactions

among the shells and PbSe in the core. The confinement of PbSe in the porous nanostructure results in blue-shifted fluorescence associated with a decrease in the fluorescence efficiency is indicated by the increased population of shallower traps along with a decrease in fluorescence lifetime in visible range. Relaxation of these shallowly trapped charge carriers to the deeper traps is further evidenced by monitoring their dynamics in NIR range.[30] A major hypothesis arrived from the previous work using Mg^{2+} [14] and the present work using Zn^{2+} is that the counterions can modulate the conformation of RNA template to varied extent and, thereby, alter the morphology of the nanostructures differently. To the best of our knowledge, this is the first report on systematic investigation of producing 3D supernanostructures of PbSe using colloidal route demonstrating both intramolecular folding and intermolecular interactions.

5. CONCLUSIONS

In the present report, Zn^{2+} ions induce the folding of RNA in RNA-mediated PbSe containing Pb^{2+} to produce a honeycomb-like porous supernanostructure. The nature of the metal ions and their binding strength with the biological moiety play an important role in the folding and self-assembly of RNA. Zn^{2+} binds to different sites of nucleotides involving purines and pyrimidine bases, in-plane $C2'-OH$, asymmetric stretches due to PO_2^{2-}, and backbone of RNA attached to PbSe. It results in the production of quantized PbSe encapsulated in the porous nanostructure which is manifested by blue-shifted fluorescence from the PbSe bound to honeycomb structure. Such porous nanosystems with optical absorption extending from UV to NIR range and fluorescence in red and NIR range may find significant applications in solar energy conversion systems, biosensing, fluorescence imaging, and drug delivery.

■ ASSOCIATED CONTENT

Ⓢ Supporting Information

Analysis of depth and pores of 2D AFM images of SB1 and SP1; 2D and 3D AFM images of PbSe containing varied $[Zn^{2+}]$; EDAX analysis of FESEM; 3D view of TEM images; Scheme S1 depicting interactions of RNA in SB1 and SP1; tables of spectral data of XPS, IR, NMR, and CD. This material is available free of charge via the Internet at http://pubs.acs.org.

■ AUTHOR INFORMATION

Corresponding Author

*E-mail: anilkfcy@iitr.ernet.in. Tel.: +91-1332-285799. Fax: +91-1332-273560.

Notes

The authors declare no competing financial interest.

■ ACKNOWLEDGMENTS

■ REFERENCES

(1) Choi, J. J.; Lim, Y.-F.; Santiago-Berrios, M. B.; Oh, M.; Hyun, B.-R.; Sun, L.; Bartnik,A. C.; Goedhart, A.; Malliaras, G. G.; Abruña, H. D. et al. *Nano Lett.* 2009, 9, 3739−3755.
(2) Hetsch, F.; Xu, X.; Wang, H.; Kershaw, S. V.; Rogach, A. L. *J. Phys. Chem. Lett.* 2011, 2, 1879−1887.
(3) Fu, H.; Tsang, S.-W. *Nanoscale* 2012, 4, 2187−2201.
(4) Kim, D. Y.; Choudhury, K. R.; Lee, J. W.; Song, D. W.; Sarasqueta, G.; So, F. *Nano Lett.* 2011, 11, 2109−2113.
(5) Pattantyus-Abraham, A. G.; Kramer, I. J.; Barkhouse, A. R.; Wang, X.; Konstantatos, G.; Debnath, R.; Levina, L.; Raabe, I; Nazeeruddin, M. K.; Grätzel, M.; et al. *ACS Nano* 2010, 4, 3374−3380.
(6) Konstantatos, G.; Sargent, E. H. *Infrared Phys. Technol.* 2011, 54, 278−282.
(7) McDonald, S. A.; Konstantatos, G.; Zhang, S.; Cyr, P. W.; Klem, E. J. D.; Levina, L.; Sargent, E. H. *Nat. Mater.* 2005, 4, 138−142.
(8) Sargent, E. H. *Adv. Mater.* 2005, 17, 515−522.
(9) Rogach, A. L.; Eychmüller, A.; Hickey, S. G.; Kershaw, S. V. *Small* 2007, 3, 536−557.
(10) Evans, C. M.; Guo, L.; Peterson, J. J.; Maccagnano-Zacher, S.; Krauss, T. D. *Nano Lett.* 2008, 8, 2896−2899.
(11) Kumar, A.; Jakhmola, A. *Langmuir* 2007, 23, 2915−2918.
(12) Kumar, A.; Jakhmola, A. *J. Phys. Chem. C* 2009, 113, 9553−9559.
(13) Kumar, A.; Singh, B. *Chem. Commun.* 2011, 47, 4144−4146.
(14) Kumar, A.; Singh, B. *RSC Adv.* 2012, 2, 9079−9090.
(15) Talapin, D. V.; Yu, H.; Shevchenko, E. V.; Lobo, A.; Murray, C. B. *J. Phys. Chem. C* 2007, 111, 14049−14054.
(16) Du, H.; Chialing, C.; Krishnan, R.; Krauss, T. D.; Harbold, J. M.; Wise, F.; Thomas, M. G.; Silcox, J. *Nano Lett.* 2002, 2, 1321−1324.
(17) Tang, J.; Sargent, E. H. *Adv. Mater.* 2011, 23, 12−29.
(18) Feldheim, D. L.; Eaton, B. E. *ACS Nano* 2007, 1, 154−159.
(19) Ma, N.; Sargent, E. H.; Kelley, S. O. *J. Mater. Chem.* 2008, 18, 954−964.
(20) Niemeyer, C. M. *Angew. Chem., Int. Ed.* 2001, 40, 4128−4158.
(21) Sotiropoulou, S.; Sierra-Sastre, Y.; Mark, S. S.; Batt, C. A. *Chem. Mater.* 2008, 20, 821−834.
(22) Ma, N.; Dooley, C. J.; Kelley, S. O. *J. Am. Chem. Soc.* 2006, 128, 12598−12599.
(23) Berti, L.; Burley, G. A. *Nat. Nanotechnol.* 2008, 3, 81−87.
(24) Coffer, J. L.; Pinizzotto, R. F.; Rho, Y. J. *NanoBiotechnol. Protocols−Springer* 2005, 303, 167−178.
(25) Levina, L.; Sukhovatkin, V.; Musikhin, S.; Cauchi, S.; Nisman, R.; Bazett-Jones, D. P.; Sargent, E. H. *Adv. Mater.* 2005, 17, 1854−1857.
(26) Ma, N.; Yang, J.; Stewart, K. M.; Kelley, S. O. *Langmuir* 2007, 23, 12783−12787.
(27) Sigel, R. K. O.; Sigel, H. A. *Acc. Chem. Res.* 2010, 43, 974−984.
(28) Ennifar, E.; Walter, P.; Dumas, P. A. *Nucleic Acids Res.* 2003, 10, 2671−2682.
(29) Vallee, B. E.; Auld, D. S. *Biochemistry* 1990, 29, 5647−5659.
(30) Details of analysis of optical and photophysical properties of RNA-mediated Zn^{2+}/PbSe nanostructures to be communicated in another MS.
(31) Joint Committee on Powder Diffraction Standards. *Inorganic Index to the Powder Diffraction File*, International Center of Diffraction Data, USA, 1998; p 02−0588.
(32) Luther, J. M.; Law, M.; Song, Q.; Perkins, C. L.; Beard, M. C.; Nozik, A. J. *ACS Nano* 2008, 2, 271−280.
(33) Sykora, M.; Koposov, A. Y.; McGuire, J. A.; Schulze, R. K.; Tretiak, O.; Pietryga, J. M.; Klimov, V. I. *ACS Nano* 2010, 4, 2021−2034.
(34) The details of this system will be published elsewhere.
(35) Banyay, M.; Sarkar, M.; Gräslunda, A. *Biophys. Chem.* 2003, 104, 477−488.
(36) Söl, D.; Nishimura, S.; Moore, P. *RNA*; Pergamon Elsevier Science (P) Ltd.: London, 2001; p 7.
(37) Sarin, P. S.; Zamecnik, P. C.; Berquist, P. L.; Scott, J. F. *Proc. Natl. Acad. Sci. U.S.A.* 1966, 55, 579−585.

(38) Ranjbar, B.; Gill, P. *Chem. Biol. Drug Des.* **2009**, *74*, 101−120.

(39) Kilina, S. V.; Craig, C. F.; Kilin, D. S.; Prezhdo, O. V. *J. Phys. Chem. C* **2007**, *111*, 4871−4878.

(40) In these experiments, $Zn^{2+}/PbSe$ was excited by 450 nm light, where Nile blue depicts negligibly small absorption. The excitation of $Zn^{2+}/PbSe$ results in the quenching of its fluorescence in both red and NIR regions along with the simultaneous production of a new peak due to the excitation of Nile blue. Within a certain range of concentrations, these spectra depicted an isoemissive point at 698 nm. A number of experiments with this system have been designed by varying the concentration of the dye. The details of this system will be published elsewhere.

5396

dx.doi.org/10.1021/jp309822w | *J. Phys. Chem. C* 2013, 117, 5386−5396